

# PIV measurements of flow past a confined cylinder

N. Adil Ozturk · Azize Akkoca · Besir Sahin

Received: 6 June 2006 / Revised: 19 December 2007 / Accepted: 19 December 2007 / Published online: 8 January 2008  
© Springer-Verlag 2008

**Abstract** This study investigates the flow past a confined circular cylinder built into a narrow rectangular duct with a Reynolds number range of  $1,500 \leq Re_d \leq 6,150$ , by employing the particle image velocimetry technique. In order to better explain the 3-D flow behaviour in the juncture regions of the lower and upper plates and the cylinder, respectively, as well as the dynamics of the horseshoe vortex system, both time-averaged and instantaneous flow data are presented for regions upstream and downstream of the cylinder. The size, intensity and interaction of the vortex systems vary substantially with the Reynolds number. Although the narrow rectangular duct with a single built-in cylinder is a geometrically symmetrical arrangement, instantaneous flow data have revealed that the flow structures in both the lower and upper plate–cylinder junction regions are not symmetrical with respect to the centreline of the flow passage. The vortical flow structures obtained in side-view planes become dominant sometimes in the lower juncture region and sometimes in the upper juncture region in unsteady mode.

## 1 Introduction

Flows around obstacles placed in rectangular ducts are a common feature of many engineering systems. They are found in heat exchangers, cooling systems for electronic components, ground–building junctions, wing–body junctions, turbine blade–rotor junctions, bridge pier–river bed junctions and external aerodynamics. Such flows are complex, 3-D, with unsteady flow features and energetic. In all of these applications, as the flow approaches the surface-mounted object, a downward flow occurs forming a horseshoe vortex which sweeps around the object’s base. As stated by Ballio et al. (1998), the presence of a horseshoe vortex system increases local shear stresses, heat transfer, drag and noise, and modifies the lift characteristics of profiles. Simpson (2001) reviewed various physical features of both laminar and turbulent junction flows around various bluff body shapes. He indicated that, except for very low Reynolds numbers, these horseshoe vortices are highly unsteady. At high Reynolds numbers they are responsible for high turbulence intensities and high surface pressure fluctuations, as well as increased heat transfer rates and erosion scours in the nose region of the obstacle.

Some investigators have classified the vortex systems formed near the juncture regions. For example, Lin et al. (2002) state that there are four different categories of vortex systems for the flow around vertical and base plate junctures. These are; (1) steady ( $400 \leq Re_w \leq 1,300$ ), (2) periodic oscillation ( $1,300 \leq Re_w \leq 1,700$ ), (3) periodic breakaway ( $1,700 \leq Re_w \leq 5,000$ ), and (4) turbulent-like vortex systems ( $5,000 \leq Re_w \leq 11,000$ ), where  $W$  is the width of square cylinder. Lin et al. (2003) also classified the horseshoe vortex systems generated near the juncture of a square cylinder and a base plate, as follows; (1) steady, (2) oscillatory, and (3) turbulence-like chaotic. The

---

N. A. Ozturk  
Faculty of Engineering and Architecture,  
Department of Mechanical Engineering,  
Mustafa Kemal University, Hatay, Turkey

A. Akkoca  
Faculty of Engineering, Department of Mechanical Engineering,  
Mersin University, Mersin, Turkey

B. Sahin (✉)  
Faculty of Engineering and Architecture,  
Department of Mechanical Engineering,  
Cukurova University, Adana, Turkey  
e-mail: bsahin@cu.edu.tr

periodical oscillatory vortex systems were further classified into three sub-categories: (1) oscillating, (2) amalgamating, and (3) breakaway vortex systems. In addition, Khan and Ahmed (2005) reported three different Reynolds-number-dependent flow regimes based on the maximum thickness,  $t$ , of the airfoil in the range of ( $2,500 \leq Re_t \leq 6,000$ ) for the vortex system upstream of a surface-mounted NACA0020 airfoil section. These regimes were: (1) a static system of vortices ( $2,000 \leq Re_t \leq 2,500$ ), where only two saddles were detected in the flow field, (2) an oscillating system of vortices ( $2,500 \leq Re_t \leq 3,500$ ), in which the number of saddles in the flow field oscillated between one and two, and (3) a shedding-splitting system of vortices ( $Re_t > 3,500$ ), where the numbers of saddles increased from two to three, and then back to two. Visbal (1991) presented computational results of both steady and periodic laminar horseshoe vortex flows generated in the region upstream of a circular cylinder/flat plate juncture for  $500 \leq Re_d \leq 5,400$ . The author also identified a new type of laminar horseshoe vortex topology.

The investigation of vortex–vortex and vortex–wall interactions upstream and downstream of the obstacles has also intrigued many researchers. Among these, Sau et al. (2003) observed that downstream extended tails of a pair of horseshoe vortices magnify the vortical structure in the far wake region, due to the presence of critical points such as saddles and nodes for a wall-mounted rectangular cylinder. Furthermore, Praisner et al. (1997) named the second horseshoe vortex formed upstream of the first one as a “tertiary vortex” in the junction region of a rectangular block, and Hwang and Yang (2004) studied the vortical structures around a wall-mounted cube placed at different locations in a channel for Reynolds numbers  $Re_h \leq 3,500$ , based on the height of the cube.

In their study, Rouvreau et al. (2005) investigated the effect of the distance between the upstream boundary and obstacle (a square block) on interactions between pressure perturbation and the boundary layer for laminar junction flow ( $Re_w = 1,000$ ), where  $W$  is the obstacle width. Kairouz and Rahai (2005) tried to control the location of the upstream separation line and reduce the axial angle of the horseshoe vortex by using a ribbed surface for a NACA0012 airfoil mounted on a flat plate. Ölçmen and Simpson (2006) examined the vortical flow structures of the NACA0020 tail wing–wall junction for  $Re = 5,940$ , based on the momentum thickness at 0.75 of the chord length, upstream of the wing on the tunnel centerline. In addition, Tseng et al. (2000) used MacCormack’s explicit predictor–corrector scheme and compared the location of the horseshoe vortex system formed in front of circular and square piers, and they reported that the domain of the horseshoe vortex in the case of the circular pier is smaller than that of the square one. Fröhlich and Rodi (2004), on

the other hand, presented large-eddy simulation (LES) results for the flow around a surface-mounted circular cylinder of a height 2.5 times the diameter for  $Re_d = 43,000$ , based on the cylinder diameter. They also presented the details of the vortical flow structures and the corresponding streamline patterns around the cylinder and detected no development of Von-Karman Street, due to the small height-to-diameter ratio,  $h/d$ . By reviewing the work of Kawamura et al. (1984), Kappler (2002), Fröhlich and Rodi (2004) stated that regular alternating vortex shedding existed for a high value of  $h/d$ , to be replaced gradually by symmetrically shed vortices for the range of  $2 \leq h/d \leq 6$ , and the researchers also observed that the vortex shedding is mostly suppressed for  $h/d < 2$ . Akilli and Rockwell (2002) investigated the vortex formation in the junction of the flat plate and circular cylinder in shallow water flow, using dye visualization and particle image velocimetry (PIV) techniques. Dye visualization revealed the formation of counter-clockwise rotating vortices just downstream of the cylinder base, within the wake region. In a similar study, Fu and Rockwell (2005a) reported that the instability of horseshoe vortices emanating from the region upstream of a vertical cylinder in a shallow water flow activates the instability of the wake flow region. In addition, Fu and Rockwell (2005b) also studied the control of vortex formation in the near wake of shallow water flow around a vertical cylinder, using a base water bleed through a very narrow slot. From these findings, the researchers concluded that a water bleed through a very small gap alters the flow structure in regions both upstream and downstream of the cylinder.

As for a tube bank located between parallel plates, the horseshoe vortex system forms in front of each cylinder and results in improved heat transfer characteristics for heat exchangers. A number of investigators, including Beale and Spalding (1999), Tsai and Sheu (1998), (1999), Rocha et al. (1997), Barsamian and Hassan (1997), Jang et al. (1996), Jang and Chen (1997), and Kundu et al. (1992) have conducted numerical calculations or simulations to investigate the flow structure and heat transfer characteristics of heat exchangers having various geometrical configurations. The time evolution of horseshoe vortices around two cylinders in tandem, and the local heat transfer coefficients on the plate surface were examined in detail by Tutar and Akkoca (2004), using FLUENT finite volume code. The researchers found that, in front of the cylinders, the horseshoe vortex enhances the heat transfer rate, whereas in the wake of the cylinders, a poor heat transfer rate occurs. The same conclusions were reported by Kim and Song (2002), (2003). Furthermore, Leu et al. (2004) used a 3-D finite difference method to study heat transfer and flow characteristics in plate fin-and-tube heat

exchangers, with vortex generators mounted behind the tubes. The Reynolds number range investigated was  $400 \leq Re_h \leq 3,000$ , based on the hydraulic diameter,  $h$ . These authors found that vortex generators further enhanced the heat transfer rates in the wake flow regions. As a result, they concluded that their vortex generators facilitated the movement of fresh fluid into the recirculating flow zone in the wake of the cylinders. The effects of variously shaped vortex generators on the heat transfer performance of heat exchangers have also been studied by several researchers, including Fiebig et al. (1995) and Biswas et al. (1996). Mendez et al. (2000) examined the effect of fin spacing on a single cylinder heat exchanger, using the dye injection technique, and showed that horseshoe vortex development depends strongly on the fin spacing and Reynolds number corresponding to the peak in the Nusselt number. Sahin et al. (2006) performed PIV experiments for Reynolds numbers in the range of  $4,000 \leq Re_d \leq 7,500$  and presented time-averaged, phase-averaged flow data and instantaneous turbulent flow statistics obtained both on the horizontal mid-plane of the flow passage and on the plan-view plane close to the lower plate surface, where  $d$  was the cylinder diameter. In addition, the formation and extension of the horseshoe vortex system in the main flow direction inside a heat exchanger flow passage have been investigated. Akkoca (2004) and Ozturk (2006) presented detailed instantaneous flow data, time-averaged flow data and heat transfer data, as well as describing the structure of the horseshoe vortex system in the heat exchanger flow passages, for various geometrical parameters.

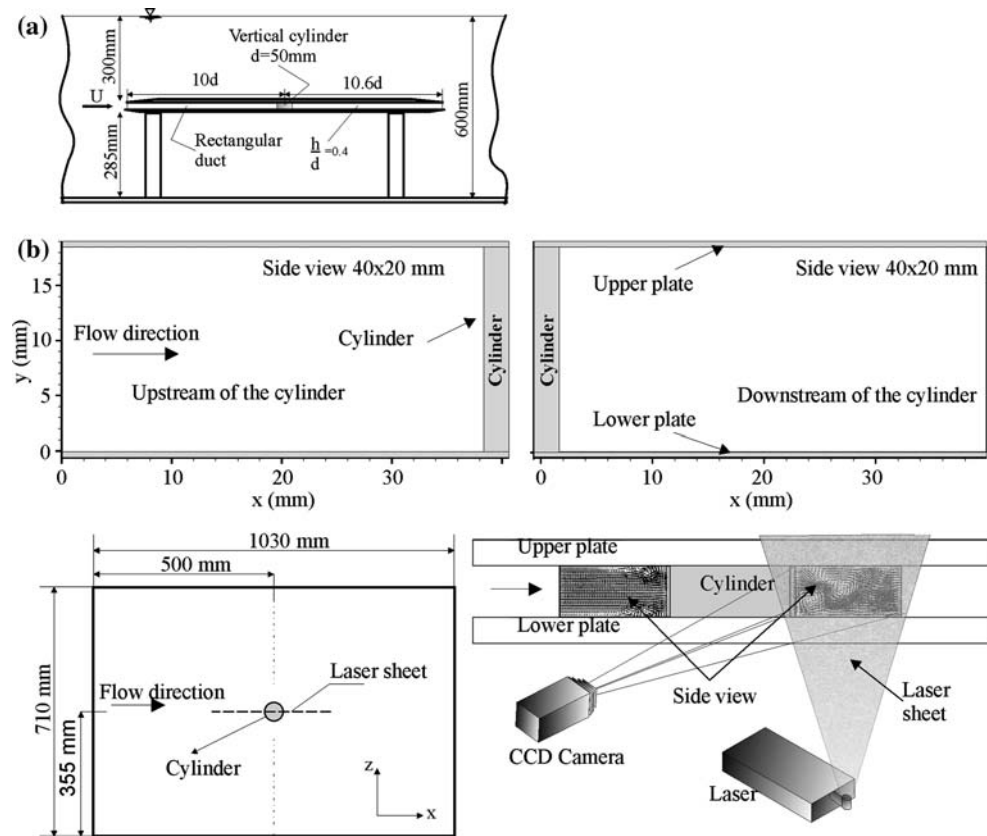
A review of research on the characteristics of junction vortex systems revealed that most of the experimental or numerical studies present time-averaged and 2-D flow statistics. There are also a few studies presenting instantaneous and phase-averaged flow results, such as those by Lin et al. (2003) and Sahin et al. (2006). In addition, most of the earlier investigators studied cylinders of various shapes (obstacles) with high aspect ratios that is, the junction vortices formed only in the lower base of the plate–cylinder. Moreover, a great number of studies have focused on the flow structure upstream of the obstacle. In the present study, as the flow approaches the confined cylinder located between two parallel plates, not only a downward flow, but also an upward flow, occurs in front of the cylinder. However, it is known that there is a strong relationship between the heat transfer rate and flow behaviour upstream and downstream of the obstacle, which is known to be both 3-D and locally unsteady. This experimental study, therefore, aims to provide insight into local time-averaged and instantaneous flow behaviour in a narrow rectangular duct with a single built-in cylinder for a range of Reynolds numbers.

## 2 Test facility

Particle image velocimetry is known to be a powerful technique for studying bluff body aerodynamics, including the capability to give quantitative information on the spatial structure of the instantaneous flow field. Therefore, in the present investigation, the PIV technique was employed to calculate the instantaneous and time-averaged flow data in the flow passage of the rectangular duct, in order to observe the local flow characteristics upstream and downstream of the cylinder.

Experiments were performed in a closed-loop free-surface water channel. Water flow was driven by a 15 kW centrifugal pump with a speed control unit. Before reaching the test chamber, water was pumped into a settling chamber and then passed through a honeycomb section and a two-to-one channel contraction in order to provide uniform free-stream velocity distributions in the range of  $15 \text{ mm/s} \leq U_\infty \leq 200 \text{ mm/s}$ . The test section of the water channel made of 15 mm-thick transparent Plexiglas had a total length of 8,000 mm a width of 1,000 mm and a depth of 750 mm. The height of the water in the test section was adjusted to 600 mm for present experiments. A schematic of the test chamber of rectangular duct with built-in cylinder shown in Fig. 1 was placed in an open water channel. Considering the earlier numerical simulations performed by Akkoca (2004), the non-dimensional distance between the lower and upper plates of the rectangular duct was selected as  $h/d = 0.4$ . Here,  $h$  is the distance between lower and upper plates,  $h = 20 \text{ mm}$ , and  $d (=50 \text{ mm})$  is the diameter of the cylinder. The length, width, and thickness of the lower and upper plates, consisting of Plexiglas sheets, were 1,030, 710, and 10 mm, respectively. The distance between the leading edge of the parallel plates and cylinder center was  $10d$ , or  $25h$  in the streamwise direction, and the downstream plate length was  $10.6d$ , measured from the center of the cylinder. Both leading and trailing edges of the plates were bevelled, in order to avoid any possible flow disturbances. The circular cylinder was glued to the upper plate and mechanically press-fitted to the lower plate. Prior to beginning formal experimentation, in order to see whether there were any flow disturbances in the cylinder–plate junction regions, the behaviour of the flow was examined in detail, using dye injection in those regions. No external flow disturbances were observed. The side-views of the test section, the position of the cylinder, the dimension of the test chamber, the location of the laser sheet and the view of camera as well as the coordinate system are shown in Fig. 1b. In the current investigation, based on the free-stream velocity and the hydraulic diameter of the rectangular duct cross-section, which has dimensions of  $20 \times 710 \text{ mm}$ , the Reynolds numbers were  $Re_{hd} = 584, 1,556$  and  $2,400$ . Reynolds numbers based on the duct

**Fig. 1** **a** Schematic diagram of the test section. **b** Side-views of the working sections in a rectangular duct with a single built-in cylinder



height were  $Re_h = 600, 1,600$  and  $2,460$ , and on the cylinder diameter were  $Re_d = 1,500, 4,000$ , and  $6,150$ , respectively.

The DPIV system consisted of a double-pulsed Nd:YAG Laser source with a wavelength of  $532\text{ nm}$ , a CCD camera with a resolution of  $1,024 \times 1,024$  pixels, a frame grabber with a maximum frame rate of  $30\text{ Hz}$ , a synchronizer and a computer. The camera was also equipped with a  $105\text{ mm}$  lens. Measurements were performed and the data processed using a Dantec Dynamics PIV system and Flow Manager Software. The image maps were read and stored using an input buffer. The images were transferred from the camera to a computer via a high-speed digital frame grabber. The laser pulses and camera were triggered with correct sequence and timing using a synchronizer. The water was seeded with neutrally buoyant silver-coated spherical particles,  $12\text{ }\mu\text{m}$  in diameter, to observe the fluid motion. The measurement plane was illuminated with a maximum laser energy output of  $120\text{ mJ/pulse}$ . The time interval between pulses was  $1.5\text{ ms}$  for all measurements. The thickness of the laser sheet illuminating the measurement plane was approximately  $1.5\text{ mm}$ . The time interval and the laser sheet thickness were selected when the maximum particle displacements in the interrogation window were obtained. The movement of the particles was recorded using a CCD camera. A frame-to-frame cross

correlation technique was used to calculate row displacement vectors. The raw velocity vector field was determined from this displacement vector field, using the time interval between laser pulses. Spurious velocity vectors were then detected applying the local median-filter technique (Westerweel 1994), and were replaced by interpolated vectors, calculated by means of a bilinear least-squares fit technique between neighbouring vectors.

Uncertainty in velocity measurements is generally caused by the seeding particle size, non-uniform particle distribution, particle overlap, interrogation window size and electronic and optical image noise (Hart 2000). In the current study, the number of particle images in an interrogation window was kept to between 15 and 20, in order to satisfy the high-image-density criterion. The size of the interrogation window was  $32 \times 32$  pixels, with 50% overlap providing 3,844 ( $62 \times 62$ ) velocity vectors over the entire field of view plane. A total of 490 instantaneous velocity vector fields were taken, with an acquisition frequency of  $10\text{ Hz}$  for each continuous run. These instantaneous flow images were captured, recorded and stored on a computer in order to get the time-averaged velocity vectors and other flow statistics. The magnification factor was determined to be 1:4.55, from the image of a millimetre scale located on the laser sheet in the flow field. This magnification factor provided an effective grid size of

0.667 × 0.667 mm in the actual physical plane of the velocity field, corresponding to 1,891 velocity vectors over the flow field of 40 × 20 mm. The digital PIV technique used in this study was similar to the one employed by Westerweel (1993), who calculated that the uncertainty in the velocity field was less than 2%. Extensive information about these uncertainty factors affecting PIV measurements was reported by Adrian (1991), Westerweel (1993), Gui et al. (2000), Hart (2000) and Adrian (2005).

### 3 Results and discussions

#### 3.1 Time-averaged experimental results upstream and downstream of the cylinder

The ultimate purpose of this study was to understand the behaviour of flow as it passed a confined circular cylinder built in to a narrow rectangular channel. Zdravitsch et al. (1994), Shah et al. (1997) and Tutar and Akkoca (2004) have reported that the flows in a narrow rectangular duct are unsteady and turbulent, and display 3-D flow characteristics.

Figure 2 illustrates the time-averaged velocity vector map,  $\langle \mathbf{V} \rangle$ , and the corresponding streamline patterns,  $\langle \psi \rangle$ , inside the narrow rectangular duct for Reynolds numbers, ( $Re_d$ ) = 1,500, 4,000, and 6,150, based on the cylinder diameter. The vertical cylinder and horizontal plates are depicted with grey tones. As the bifurcating streamlines of the main flow approach the upstream surface of the vertical cylinder, the main flow is further divided into two subsidiary flows. The division starts from the half-saddle point of the attachment,  $S_{ab}$  indicated by a small arrow, which is located on the cylinder surface at the central line of the horizontal plane. One part of the flow is oriented towards the lower plate, the other towards the upper plate, forming two symmetrical horseshoe vortex systems.  $S_{ab}$  moves upward and downward in the vertical direction along the surface of the vertical cylinder. The time-averaged flow data reveal that the flow structure is symmetric with respect to the centreline ( $y = 10$  mm), passing through  $S_{ab}$  for all values of Reynolds numbers. Time-averaged patterns of streamlines indicate that the reversing flow starts from half-node of attachment,  $N_a$ , and occurs on both plate surfaces. In the current work, the topological descriptions stated by Visbal (1991), Ballio and Franzetti (2000) and Khan and Ahmed (2005) were used. The domains of horseshoe vortex systems cover a region between the half-saddle of attachment,  $S_{ab}$ , located on the cylinder surface, and half-node of attachment,  $N_a$ , placed on the lower and upper plate surfaces. The primary foci (horseshoe vortices),  $F_1$ , appear in the vicinity of the lower plate–cylinder junction and rotate clockwise, while

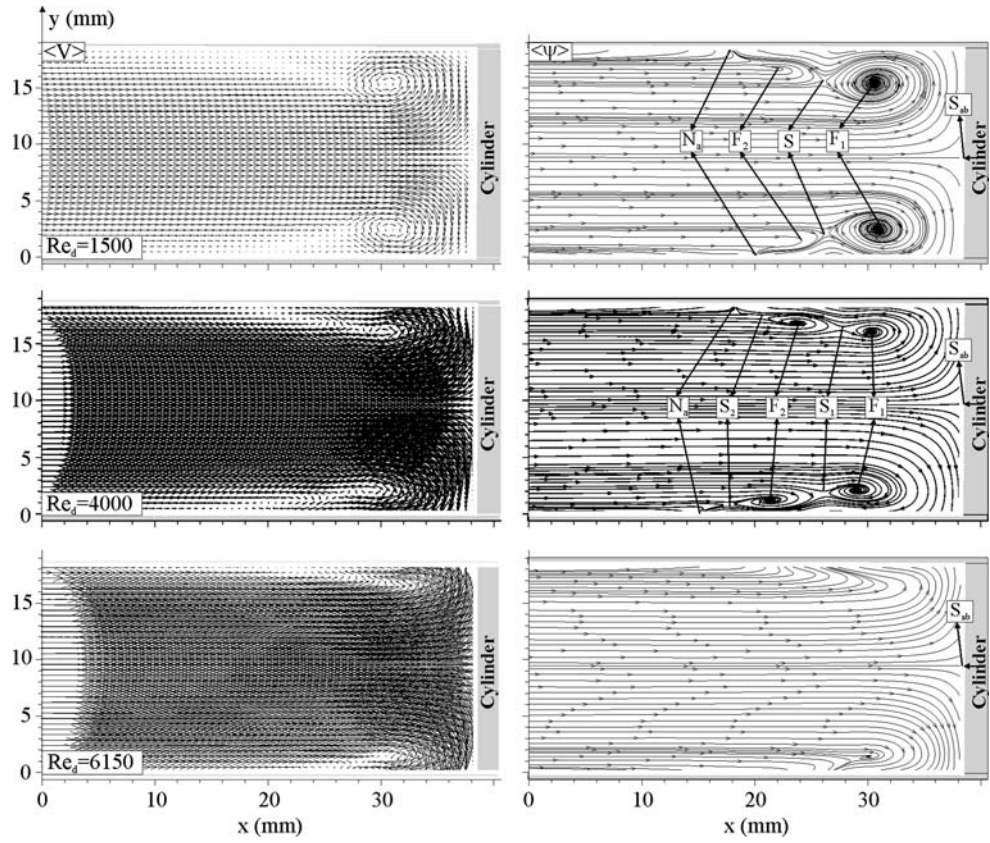
the others, in the vicinity of the upper plate–cylinder junction, rotate counter-clockwise for all Reynolds numbers investigated. The domains of the primary foci (horseshoe vortices),  $F_1$ , get smaller as the Reynolds number increases, which is due to the higher rate of momentum of the incoming flow. Developing foci (horseshoe vortices),  $F_2$ , located upstream of the primary horseshoe vortices,  $F_1$ , are also observed for  $Re_d = 1,500$  and  $Re_d = 4,000$ . The magnitudes of the incoming horseshoe vortices (foci),  $F_2$ , increase with the Reynolds number from  $Re_d = 1,500$  to  $Re_d = 4,000$ . For  $Re_d = 6,150$ , a relatively small domain of the primary horseshoe vortex,  $F_1$ , is detected near the cylinder–lower plate junction region. However, no incoming or developing horseshoe vortex is observed. Here, the saddle points located between the primary and developing horseshoe vortices are designated with  $S$  in Fig. 2.

Fig. 3 illustrates the time-averaged velocity vector map,  $\langle \mathbf{V} \rangle$ , and the corresponding streamline patterns,  $\langle \psi \rangle$ , downstream of the cylinder. The flow separation, which occurs on both sides of the cylinder, causes the formation of a flow re-circulation region in the cylinder wake, which results in a decreased heat transfer rate in this region. This has also been reported by Jang et al. (1996) and Meinders and Hanjalic (2002). The size of the wake region decreases as the Reynolds number increases. Downstream of the cylinder, two symmetric foci,  $F_1$ , having clockwise and counter-clockwise directions of rotation are observed close to the upper and lower junction regions, respectively. These foci,  $F_1$ , emerge from a critical point located on the plate surfaces which Tsai and Sheu (1998) called the “repelling critical point.” Alternatively, Visbal (1991) named this critical point as a “half-node of attachment.” The exact position of this critical point was out of the field of view of the PIV measurements for the current experiments. The parallel streamlines, which converge as if they emerge from these critical points on both lower and upper plates farther downstream of the cylinder, reveal the presence of these critical points for  $Re = 6,150$ . As the streamlines approach the cylinder surface, they feed into two symmetric counter-rotating vortices. Numerical results of Tutar and Akkoca (2004) presented similar released flows enforced by a horseshoe vortex system. Using dye visualization, Akilli and Rockwell (2002) visualized counter-clockwise rotating vortices downstream from the base of the cylinder in shallow water flow. For all values of Reynolds number, the time-averaged flow data reveal that downstream of the cylinder, the flow pattern is symmetrical with respect to the centreline. Incoming foci (developing vortices),  $F_2$ , are detected only for  $Re_d = 4,000$ , downstream of the cylinder.

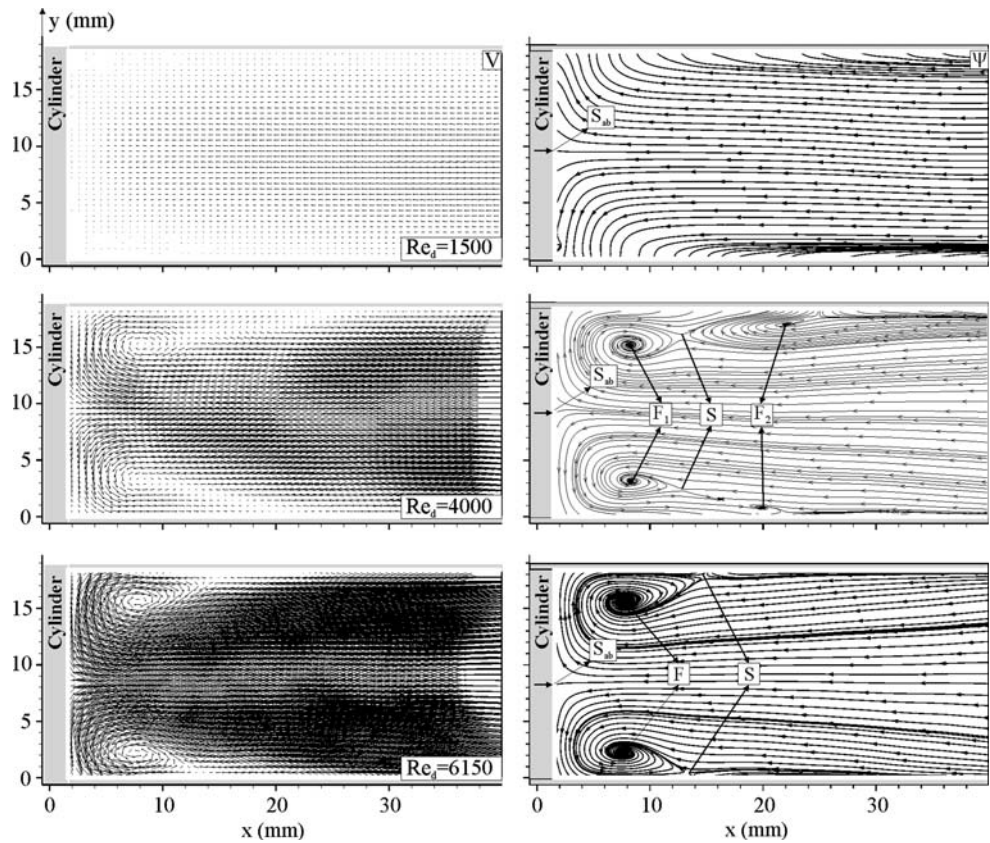
Figure 4 presents the time-averaged normalized vorticity contours,  $\langle \omega d/U \rangle$ , upstream and downstream of the



**Fig. 2** Time-averaged velocity vectors,  $\langle \mathbf{V} \rangle$ , map and corresponding patterns of streamlines,  $\langle \psi \rangle$ , upstream of the cylinder



**Fig. 3** Time-averaged velocity vectors,  $\langle \mathbf{V} \rangle$ , map and corresponding patterns of streamlines,  $\langle \psi \rangle$ , downstream of the cylinder



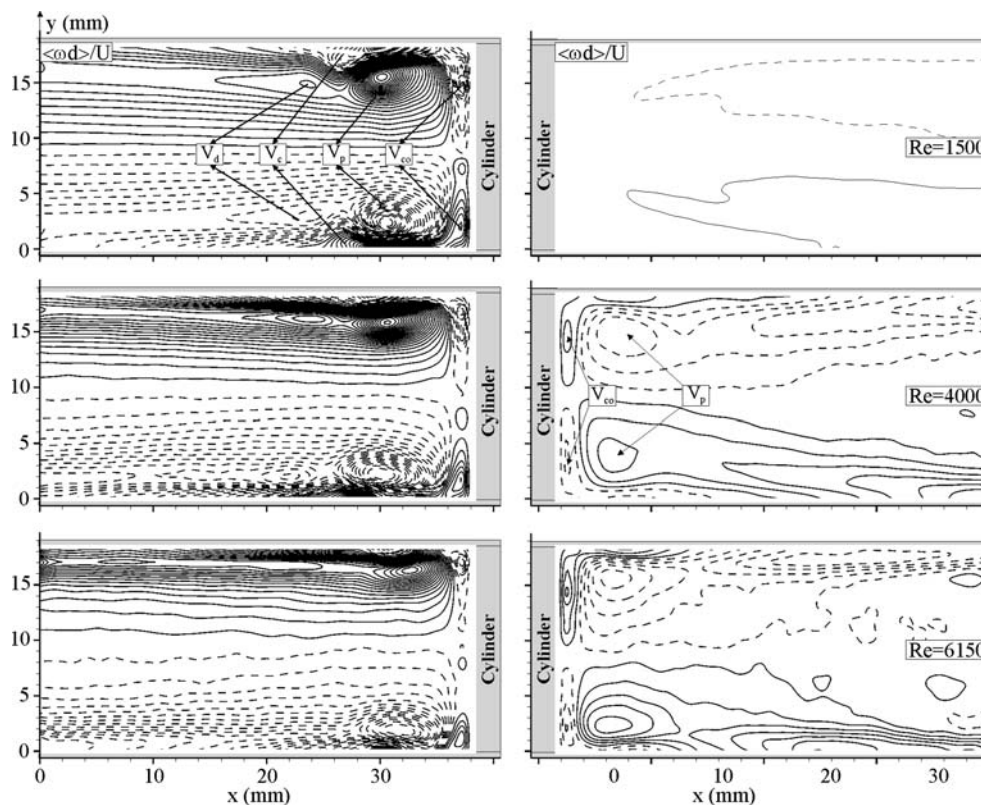
cylinder for  $Re_d = 1,500, 4,000, \text{ and } 6,150$ , respectively. The images in the left and right columns indicate the normalized vorticity contours upstream and downstream of the cylinder, respectively. The positive and negative contours are displayed with solid and dashed lines, respectively. Two symmetric primary vortices,  $V_p$ , and a pair of corner vortices,  $V_{co}$ , are located at the upper and lower junction regions. A pair of counter-rotating vortices,  $V_c$ , located between the primary,  $V_p$ , and developing,  $V_d$ , vortices, are also distinctly present upstream of the cylinder for  $Re_d = 1,500$ . The domain of primary vortices,  $V_p$ , developing vortices,  $V_d$ , and corner vortices,  $V_{co}$ , upstream of the cylinder decrease as the Reynolds number is increased. As the sizes of the corner vortices get smaller with an increase in Reynolds number, the centres of the primary vortices shift further down towards the cylinder. The animation of 490 images has demonstrated that negative and positive primary vortices located at the lower and upper plate surfaces,  $V_p$ , split up and form corner vortices,  $V_{co}$ , with similar sign. In other words, the corner vortices,  $V_{co}$ , are fed by the primary vortices,  $V_p$ . Downstream of the cylinder, both the primary and corner vortices become stronger as the Reynolds number is increased.

Figure 5 illustrates the time-averaged normalized Reynolds stress correlations,  $\langle u'v' \rangle / U^2$ , and the distributions of streamwise and transverse velocities,  $u/U$  and  $v/U$ , for  $Re_d = 1,500$  across the flow passage. The images in the

left and right columns indicate the time-averaged flow data upstream and downstream of the cylinder, respectively. The minimum and incremental values of each variable are also indicated in the images. Three pairs of concentrated time-averaged normalized Reynolds stress correlations,  $\langle u'v' \rangle / U^2$ , in the upstream vicinity of the cylinder–plate junctions were observed as shown in the first row of Fig. 5. The concentrations indicated by  $C_p, C_c$  and  $C_d$  represent primary, counter-rotating, and developing time-averaged flow data contours. The locations of the peak values of these concentrations indicate that these regions exhibit high fluctuations which are caused by the primary,  $V_p$ , counter-rotating,  $V_c$ , and developing,  $V_d$ , vortices along the shear layers indicated in Fig. 4. The vortices designated by  $V_c$  rotate with a sign opposite that of the primary,  $V_p$ , and developing vortices,  $V_d$ . These contours represent fluctuating regions resulting from the corner vortex. Fluctuating flow regions downstream of the cylinder are not detected due to the low values of velocity and the absence of strong vortices.

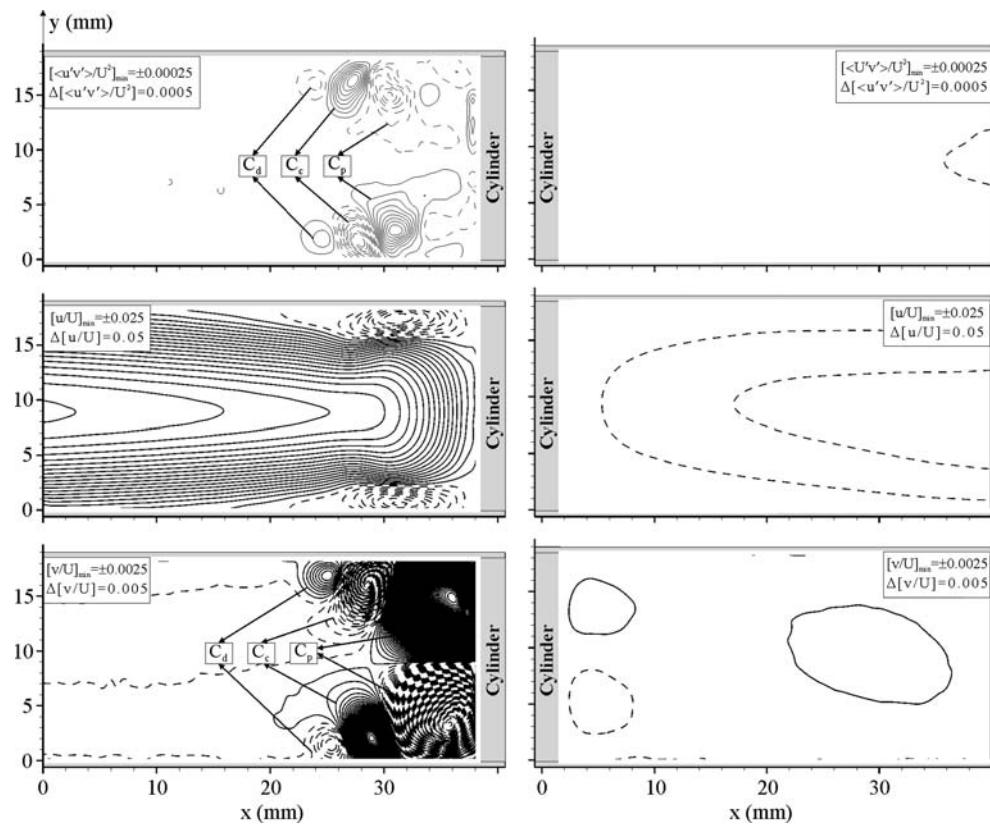
There are two negative streamwise velocity,  $(u/U)$ , concentrations located in the vicinity of the lower and upper junction regions upstream of the cylinder, as seen in Fig. 5. The peak value of the positive streamwise velocity concentration is out of the field of view of PIV measurements. Three symmetric pairs of transverse velocity,  $(v/U)$ , concentrations ( $C_p, C_c$  and  $C_d$ ) are seen to be adjacent,

**Fig. 4** Time-averaged normalized vorticity contours upstream and downstream of the cylinder. Minimum and incremental values of vorticity are  $\langle \omega_{\min} d \rangle / U = \pm 0.5$  and  $\Delta[\langle \omega d \rangle / U] = 1$





**Fig. 5** Time-averaged normalized Reynolds stress correlations,  $\langle u'v' \rangle / U^2$ , contours of streamwise velocity,  $u/U$ , and transverse velocity,  $v/U$ , upstream and downstream of the cylinder for  $Re_d = 1,500$



lined up back-to-back, and in close proximity to the junction region upstream of the cylinder, as shown in the last row of Fig. 5; these correspond to the primary,  $V_p$  ( $C_p$ ), counter-rotating,  $V_c$  ( $C_c$ ), and developing vortices,  $V_d$  ( $C_d$ ), as seen in the first image of Fig. 4. Downstream of the cylinder, no particular concentration features are apparent for the case of  $Re_d = 1,500$ , as shown in the right hand column of Fig. 5.

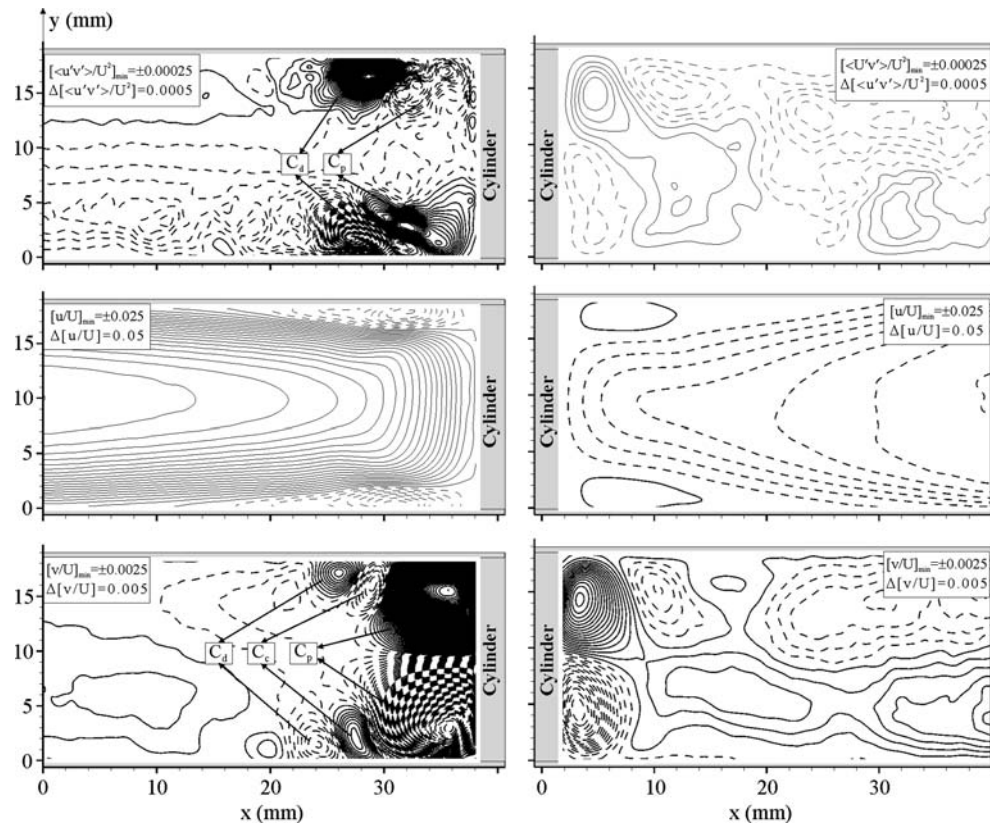
Figure 6 illustrates the time-averaged normalized Reynolds stress correlations,  $\langle u'v' \rangle / U^2$ , the distributions of streamwise and transverse velocities, ( $u/U$  and  $v/U$ ), for  $Re_d = 4,000$  in side-view planes across the flow passage, in both regions upstream and downstream of the cylinder. A cross-comparison of the flow statistics shown in Figs. 5 and 6 reveals that in the upstream region of the cylinder, the locations of the peak values of normalized Reynolds stress correlations,  $\langle u'v' \rangle / U^2$ , the distributions of streamwise velocity,  $u/U$ , and the transverse velocity,  $v/U$ , shift towards the upstream face of the cylinder as the Reynolds number increases. It was also observed that the strength of the flow characteristics downstream of the cylinder, indicated in Figs. 5 and 6, increases as a function of Reynolds number. This is associated with the formation of rotating vortices downstream of the cylinder, as shown in the images in Fig. 3 and in the last row of Fig. 4.

### 3.2 Instantaneous flow data upstream and downstream of the cylinder

Merely examining the time-averaged flow data cannot reveal whether the flow structure formed in the narrow rectangular ducts is symmetric, with respect to the centre line of the flow passage. Thus, in order to better understand the main flow evolution, as well as the flow interactions inside the rectangular duct, instantaneous velocity vector,  $\mathbf{V}$ , maps upstream of the cylinder are presented in Fig. 7 for  $Re_d = 4,000$  and for consecutive frames, between  $N = 100$  and  $N = 111$ , selected from among the 490 instantaneous images. For  $N = 100$ , two identical developing large-scale swirling patterns of velocity vectors of approximately the same length, are observed close to the lower plate surface, and relatively wide and elongated primary swirls of velocity were detected close to the upper plate surface. The well-defined twin swirls of velocity vectors rotate clockwise, while the elongated vortex rotates counter-clockwise. A line of velocity vectors attached perpendicularly to the surface of the vertical cylinder (shown by an arrow) are located below the centreline ( $y = 10$  mm) of the flow passage, indicating that the vortical flow structure is dominant above the centreline ( $y = 10$  mm), as seen in the image of  $N = 100$ . This line of velocity vectors corresponds to the bifurcating



**Fig. 6** Time-averaged normalized Reynolds stress correlations,  $\langle u'v' \rangle / U^2$ , contours of streamwise velocity,  $u/U$ , and transverse velocity,  $v/U$ , velocities, upstream and downstream of the cylinder, for  $Re_d = 4,000$

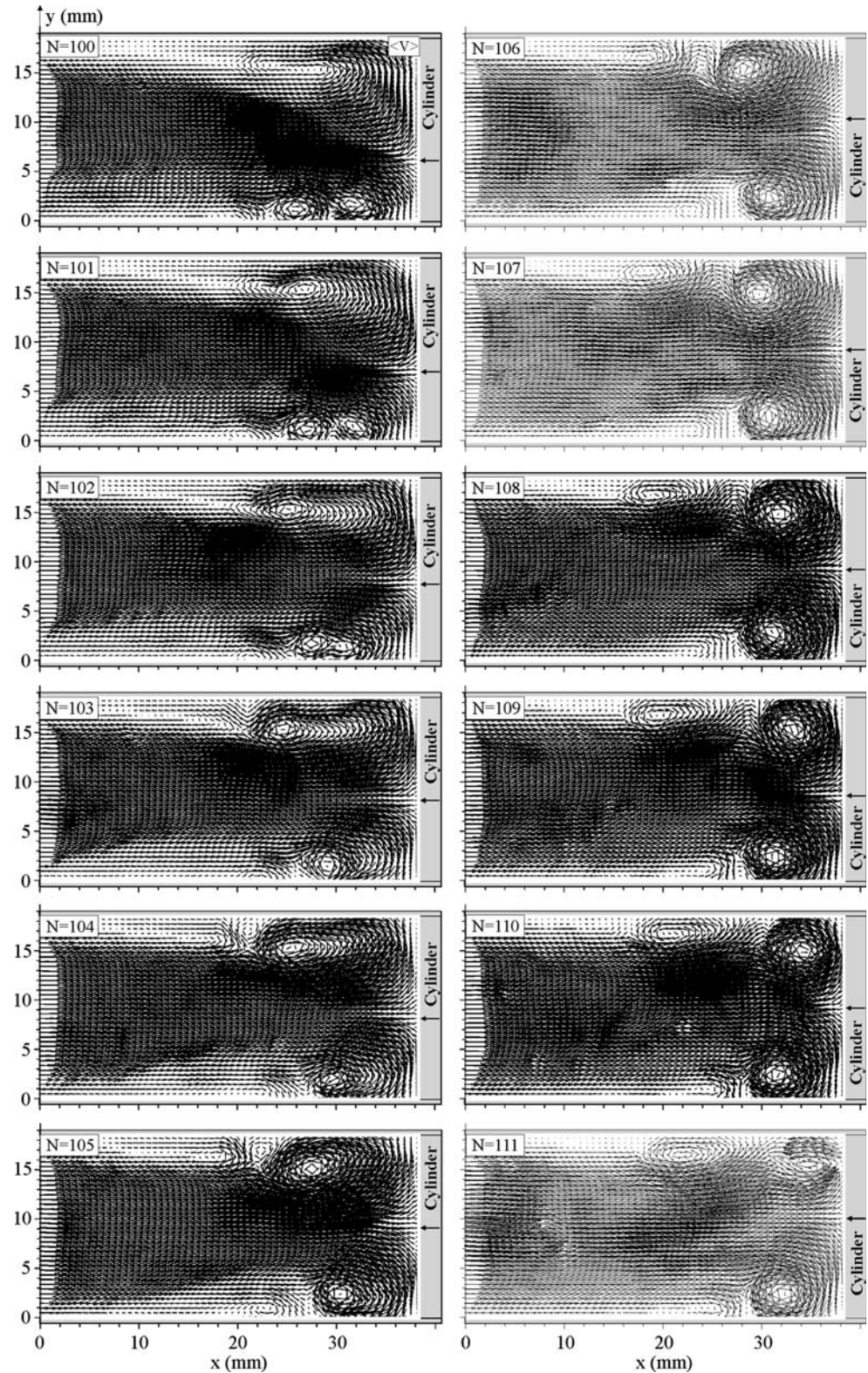


streamline attached to the surface of the cylinder, forming a half-saddle point of attachment,  $S_{ab}$ , shown in Fig. 2. In the second image, close to the lower plate for  $N = 101$ , the developing large-scale swirls of velocity vectors become stronger, and primary swirls of these vectors close to the upper plate are about to combine with another small-scale swirl located upstream of it. In the third image, for  $N = 102$ , the well-defined twin swirls of velocity vectors,  $\mathbf{V}$ , located close to the lower plate surface, and two swirls of velocity vectors,  $\mathbf{V}$ , located close to the upper plate surface, begin to combine with each other. In the fourth image, for  $N = 103$ , the primary swirls of velocity vectors,  $\mathbf{V}$ , develop and get stronger, and counter-rotating vortices appear close to the upper plate. Close to the lower plate surface, relatively well-defined swirls of velocity vectors,  $\mathbf{V}$ , are formed as a result of coalescence of the twin swirls of velocity vectors observed in the previous frames. In the fifth and sixth images, for  $N = 104$  and  $105$ , close to the upper plate, the size as well as strength of the counter-rotating and developing swirls of velocity vectors increase. It is known that whenever the counter-rotating swirls of velocity vectors begin to decay, the developing swirls,  $\mathbf{V}$ , start to move towards the primary swirling patterns,  $\mathbf{V}$ , in the main flow direction. Inversely, as the counter-rotating swirls of velocity vectors grow in size, it constrains the developing swirls,  $\mathbf{V}$ , to move towards well-defined swirls,  $\mathbf{V}$ . Close to the lower plate surface, the centre of the

primary vortex begins to move towards the cylinder–lower plate junction. Between  $N = 106$  and  $N = 111$ , close to the upper plate the central points of the primary swirls of velocity vectors shift towards the cylinder–upper plate junction; the relatively well-defined counter-rotating, swirls of velocity decay, and the developing swirls of velocity become stronger and propagate along the upper plate surface as time progresses. Below the centreline ( $y = 10$  mm) of the flow passage, the position of the primary swirls of velocity remains nearly unchanged, whereas the centre of the developing swirls of velocity moves towards the primary one, as a result of the decay of the counter-rotating swirls of velocity. The primary swirls of velocity with opposite rotations which appear near both the upper and lower plate–cylinder junctions, become nearly symmetric in the images  $N = 107$  and  $108$ .

Figure 8 presents instantaneous velocity vectors,  $\mathbf{V}$ , streamline patterns,  $\psi$ , and corresponding vorticity contours,  $\omega$ , upstream of the cylinder for the image frame numbers  $N = 268, 329, 400$ , and  $453$ , chosen from among the set of 490 instantaneous images. For  $N = 268$ , a half-saddle of attachment,  $S_{ab}$ , is detected above the centerline ( $y = 10$  mm) of the flow passage. The main flows above and below this half-saddle,  $S_{ab}$ , move in an asymmetrical manner. The primary focus,  $F_p$ , located in the vicinity of the lower plate, is stronger and located farther from the upstream face of the cylinder, comparing to the one

**Fig. 7** Instantaneous velocity vectors,  $V$ , map upstream of the cylinder for  $Re_d = 4,000$



obtained in the vicinity of the upper plate. A very strong secondary or counter-rotating focus,  $F_c$ , having an opposite rotation according to the primary and the developing foci,  $F_p$  and  $F_d$ , bursts from the surface of the lower and upper

plates. Below the centreline of the flow passage, the vortical flow structure is more dominant, and foci are found to be stronger in the region close to the lower plate, compared with those located close to the upper plate. Inside the flow



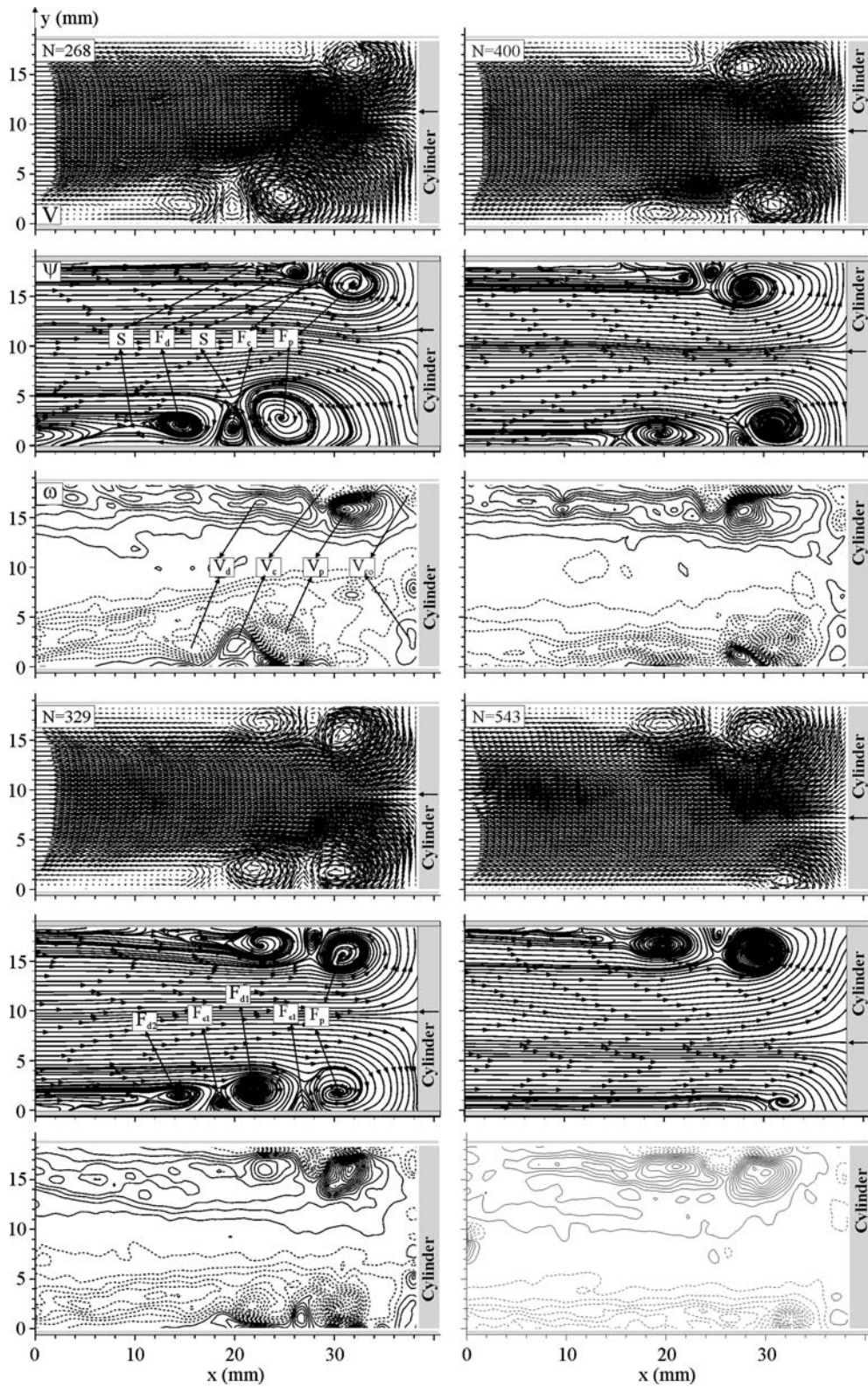
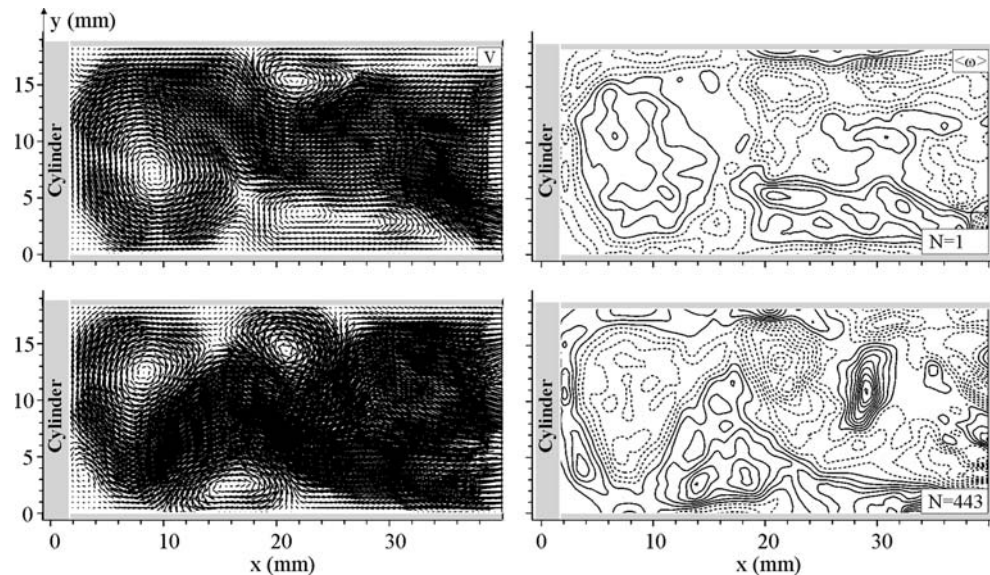


**Fig. 8** Instantaneous velocity vectors,  $V$ , map patterns of streamlines,  $\psi$ , and corresponding vorticity contours,  $\omega$ , upstream of the cylinder for  $Re_d = 4,000$

**Fig. 9** Instantaneous velocity vectors map,  $V$ , and vorticity,  $\omega$ , downstream of the cylinder for  $Re_d = 4,000$



passage, a larger size of separated flow region forms along the lower plate surface, compared with the upper plate surface. In the vorticity contours field,  $V_{co}$ ,  $V_p$ ,  $V_c$ , and  $V_d$  denote the corner, primary, counter-rotating, and developing vortices, respectively. For  $N = 329$ , the main flows above and below the half-saddle of attachment,  $S_{ab}$ , are found to be nearly symmetric, and the developing vortices are found to be as strong as the primary vortices. There are two counter-rotating foci,  $F_{c1}$  and  $F_{c2}$ , located between the primary foci,  $F_p$ , and developing foci,  $F_{d1}$ , and between the two developing foci,  $F_{d1}$  and  $F_{d2}$ , as observed in the vicinity of the lower plate. These foci can also be identified as horseshoe vortices. In the image  $N = 400$  the centre of the primary vortex below the centreline ( $y = 10$  mm) of the flow passage is found to be closer to the upstream face of the cylinder, when compared to the one above the centreline. The developing vortex observed in the vicinity of the lower plate surface is stronger than the one located in the vicinity of the upper plate surface. For  $N = 453$ , the half-saddle of attachment,  $S_{ab}$ , is located below the centreline ( $y = 10$  mm) of the flow passage, and the vortical flow structure is found to be dominant in the vicinity of the upper plate surface, where the developing vortex is found to be as strong as the primary one. A counter-rotating vortex,  $V_c$ , and a developing vortex,  $V_d$ , are also detected in region close to the upper plate surface. Only a localized primary vortex,  $V_p$ , placed close to the lower plate surface, is observed. When the animations are observed it is seen that the half-saddle of attachment,  $S_{ab}$ , moves vertically up and down along the surface of the cylinder. The vertical displacement of the point  $S_{ab}$  becomes very small for  $Re_d = 1,500$ , whereas it becomes very large and moves faster for  $Re_d = 6,150$ .

Downstream of the cylinder, very complex instantaneous flow patterns are captured for  $Re_d = 4,000$  as shown

in Fig. 9. In the first row of the images, downstream of the cylinder there is a very large primary vortex rotating counter-clockwise, surrounded by a clockwise rotating vortex, as seen in the first row of images in Fig. 9. In the second row of images, the opposite flow rotations occur. The animation of the 490 images indicates that separate flow regions in the vicinity of both the plates and the cylinder junctions rotate unsteadily, sometimes clockwise and sometimes counter-clockwise; this reveals that the wake flow structure downstream of the cylinder is strongly 3-D and energetic. If the instantaneous flow data are examined in detail, it can be seen that spiralling horseshoe vortices roll into the wake flow region, causing the wake flow to reverse towards the vertical cylinder. As this flow approaches the cylinder, it begins to rotate along the lower and upper plates surfaces. Thus, this confined cylinder geometry increases the rotation of these vortices to a higher level.

#### 4 Conclusion

There has been a growth of interest in understanding more fully the formation and behaviour of local flow structures in narrow rectangular ducts. In this study, using time-averaged and instantaneous flow statistics obtained by use of the PIV technique, the general features of the flow and particularly the horseshoe vortex mechanism were investigated in detail for Reynolds numbers in the range  $1,500 \leq Re_d \leq 6,150$ , and for a non-dimensional distance between the lower and upper plate surfaces of  $(h/d) = 0.4$ .

Both upstream and downstream of the cylinder, the flow structure is highly 3-D and complex. The main flow separates, starting from a critical point located on the lower and upper plate surfaces, in the regions upstream and



downstream of the cylinder. As the main flow approaches the vertical cylinder, a half-saddle of attachment occurs on the surface of the cylinder, orienting toward the upper and the lower plates and forming the horseshoe vortices. The size and the strength of the primary, developing, and corner vortices change rapidly, depending on the value of the Reynolds number. The primary horseshoe vortex system,  $V_p$ , formed in the vicinity of the cylinder–plate junction region, is located between the corner vortex,  $V_{co}$ , and the counter-rotating vortex,  $V_c$ . The corner vortex,  $V_{co}$ , prevents the primary horseshoe vortex,  $V_p$ , from moving further downstream towards the cylinder surface, while the counter-rotating vortex,  $V_c$ , prevents the developing and primary horseshoe vortices,  $V_d$  and  $V_p$ , from continuously interacting with each other. As the Reynolds number increases, the locations of the peak values of the Reynolds stress correlations,  $((u'v')/U^2)$ , shift towards the cylinder surface in the upstream region of the flow. The instantaneous flow structures are not symmetric with respect to the centreline of the flow passage. The location, size, strength, intensity and number of vortices vary with time in random motion. The vortical flow structure occasionally becomes dominant both above and below the centreline of the flow passage. A half-saddle of attachment,  $S_{ab}$ , occurring on the cylinder surface, travels arbitrarily and vertically up and down. The displacement rate of this half-saddle of attachment,  $S_{ab}$ , depends on the Reynolds number. The data obtained in this study also reveal that flow structures downstream of the cylinder are also complex. For example, reversed flow rotates unsteadily, sometimes clockwise and sometimes counter-clockwise, making the flow structures rather energetic, which strongly affect the heat and mass transfer characteristics downstream of the cylinder.

**Acknowledgments** The authors acknowledge the financial support of the Office of Scientific Research Projects of Cukurova University for funding under contract No: AAP20025 and MMF.2004.BAB.13. The authors also wish to thank Professor Colin Clark for editing the manuscript.

## References

- Adrian RJ (1991) Particle-imaging techniques for experimental fluid mechanics. *Annu Rev Fluid Mech* 23:261–304
- Adrian RJ (2005) Twenty years of particle image velocimetry. *Exp Fluids* 39:159–169
- Akilli H, Rockwell D (2002) Vortex formation from a cylinder in shallow water. *Phys Fluids* 14:2957–2967
- Akkoca A (2004) Computational modeling of turbulent heat transfer in plate fin-and-tube heat exchangers, PhD thesis, Department of Mechanical Engineering, Institute of Natural and Applied Sciences, Cukurova University, Adana, Turkey
- Ballio F, Franzetti S (2000) Topological analysis of a junction vortex flow. *Advances in Fluid Mechanics*, 255–264
- Ballio F, Guadagnini A, Malavasi S (1998) Stresses due to a horseshoe vortex at a surface-cylinder intersection. In: International communications in heat exchanger symposium (poster session, 31.08.1998, 12:00–12:15)
- Barsamian HR, Hassan YA (1997) Large eddy simulation of turbulent crossflow in tube bundles. *Nucl Eng Des* 172:103–122
- Beale SB, Spalding DB (1999) A numerical study of unsteady fluid flow in in-line and staggered tube banks. *J Fluids Struct* 13:723–754
- Biswas G, Torii K, Fujii D, Nishino K (1996) Numerical and experimental determination of flow structure and heat transfer effects of longitudinal vortices in channel flow. *Int J Heat Mass Transf* 39:3441–3451
- Fiebig M, Guntermann H, Mitra NK (1995) Numerical analysis of heat transfer and flow loss in a parallel plate heat exchanger element with longitudinal vortex generators as fins. *J Heat Transf* 117:1064–1067
- Frölich J, Rodi W (2004) LES of the flow around a circular cylinder of finite height. *Int J Heat Fluid Flow* 25:537–548
- Fu H, Rockwell D (2005a) Shallow flow past a cylinder: transition phenomena at low Reynolds number. *J Fluid Mech* 540:75–97
- Fu H, Rockwell D (2005b) Shallow flow past a cylinder: control of the near wake. *J Fluid Mech* 539:1–24
- Gui L, Merzkirch W, Fei R (2000) A digital mask technique for reducing the bias error of the correction-based PIV interrogation algorithm. *Exp Fluids* 29(1):30–35
- Hart DP (2000) PIV error correction. *Exp Fluids* 29:13–22
- Hwang JY, Yang KS (2004) numerical study of vortical structures around a wall-mounted cubic obstacle in channel flow. *Phys Fluids* 16(7):2382–2394
- Jang JY, Chen LK (1997) Numerical analysis of heat transfer and fluid flow in a three-dimensional wavy fin-and-tube heat exchanger. *Int J Heat Mass Transf* 40(16):3981–3990
- Jang JY, Wu MC, Chang WJ (1996) Numerical and experimental studies of three-dimensional plate fin-and-tube heat exchangers. *Int J Heat Mass Transf* 39(14):3057–3066
- Kairouz KA, Rahai HR (2005) Turbulent junction flow with an upstream ribbed surface. *Int J Heat Fluid Flow* 26:771–779
- Kappler M (2002) Experimentelle untersuchung der umstromung von kreiszylindern mit ausgeprägt dreidimensionalen effekten. Ph.D. thesis, Institute for Hydromechanics, University of Karlsruhe
- Kawamura T, Hiwada M, Hibino T, Mabuchi I, Kamuda M (1984) Flow around a finite circular cylinder on a flat plate. *Bull JSME* 27(232):2142–2151
- Khan MJ, Ahmed A (2005) Topological model of flow regimes in the plane of symmetry of a surface-mounted obstacle. *Phys Fluids* 17(1–8):045101
- Kim JY, Song TH (2002) Microscopic phenomena and macroscopic evaluation of heat transfer from plate fins/circular tube assembly using naphthalene sublimation technique. *Int J Heat Mass Transf* 45:3397–3404
- Kim JY, Song TH (2003) Effect of tube alignment on the heat/mass transfer from a plate fin and two-tube assembly: naphthalene sublimation results. *Int J Heat Mass Transf* 46:3051–3059
- Kundu D, Skeikh AH, Lou DYS (1992) Heat transfer in crossflow over cylinders between two parallel plates. *Numer Heat Transf Part A* 114:558–564
- Leu JS, Wu YH, Jang JY (2004) Heat transfer and fluid flow analysis in plate fin-and-tube heat exchangers with a pair of block shape vortex generators. *Int J Heat Mass Transf* 47:4327–4338
- Lin C, Chiu PH, Shieh SJ (2002) Characteristics of horseshoe vortex system near a vertical plate-base plate juncture. *Exp Therm Fluid Sci* 27:25–46
- Lin C, Lai WJ, Chang KA (2003) Simultaneous particle image velocimetry and laser Doppler velocimetry measurements of periodical oscillatory horseshoe vortex system near square cylinder-base plate juncture. *J. Eng Mech* 129(10):1173–1188

- Meinders ER, Hanjalic K (2002) Experimental study of convective heat transfer from in-lined and staggered configurations of two wall-mounted cubes. *Int J Heat Mass Transf* 45:465–482
- Mendez RR, Sen M, Yang KT, McClain R (2000) Effect of fin spacing on convection in a plate fin-and-tube heat exchanger. *Int J Heat Mass Transf* 43:39–51
- Ölçmen SM, Simpson RL (2006) Some features of a turbulent wing-body junction vertical flow. *Int J Heat Fluid Flow* 27:980–993
- Ozturk NA (2006) Investigation of flow characteristics in heat exchangers of various geometries. PhD thesis, Department of Mechanical Engineering, Institute of Natural and Applied Sciences, Cukurova University, Adana, Turkey
- Praisner TJ, Seal CV, Takmaz L, Smith CR (1997) Spatial-temporal turbulent flow field and heat transfer behavior in end-wall junctions. *Int J Heat Fluid Flow* 18:142–151
- Rocha LAO, Saboya FEM, Vargas JVC (1997) A comparative study of elliptical and circular sections in one- and two-row tubes and plate fin heat exchangers. *Int J Heat Fluid Flow* 18:247–252
- Rouvreau S, David L, Calluau D, Joulain P (2005) Laminar junction flow at low Reynolds number: influence of the upstream region on the comparison between experiments and calculations. *CR Mech* 333:265–272
- Sahin B, Akkoca A, Ozturk NA, Akilli H (2006) Investigations of flow characteristics in a plate fin-and-tube heat exchanger model composed of single cylinder. *Int J Heat Fluid Flow* 27:522–530
- Sau A, Hwang RR, Sheu TWH, Yang WC (2003) Interaction of trailing vortices in the wake of wall-mounted rectangular cylinder. *Phys Rev E* 68(1–15):056303
- Shah RK, Heikal MR, Thonon B (1997) Advances in numerical analysis of fluid flow, heat transfer, and flow friction characteristics of compact heat exchanger surfaces. In: Proceedings of international symposium on fluid flow and heat transfer, Ankara, Turkey, pp 68–87
- Simpson RL (2001) Junction flows. *Annu Rev Fluid Mech* 33:415–443
- Tsai SF, Sheu TWH (1998) Some Physical insights into a two-row finned tube heat transfer. *Comput Fluids* 27(1):29–46
- Tsai SF, Sheu TWH (1999) Heat transfer in a conjugate heat exchanger with a wavy fin surface. *Int J Heat Mass Transf* 42:1735–1745
- Tseng MH, Yen CL, Song CCS (2000) Computation of three-dimensional flow around square and circular piers. *Int J Numer Methods Fluids* 34:207–227
- Tutar M, Akkoca A (2004). Numerical analysis of fluid flow and heat transfer characteristics in three dimensional plate fin-and-tube heat exchangers. *Numer Heat Transf Part A* 46:301–321
- Visbal MR (1991) Structure of laminar juncture flows. *AIAA J* 29(8):1273–1282
- Westerweel J (1993) Digital particle image velocimetry, theory and application, Delft University Press
- Westerweel J (1994) Efficient detection of spurious vectors in particle image velocimetry data sets. *Exp Fluids* 16:236–247
- Zdravitsch F, Fletcher CAJ, Behnia M (1994) Laminar and turbulent heat transfer predictions in tube banks in cross flow. In: Proceedings of international conference on fluid and thermal energy conversion, Indonesia, 12–16